

Near-Infrared Ternary Tandem Solar Cells

Yongxi Li, Jiu-Dong Lin, Xiao Liu, Yue Qu, Fu-Peng Wu, Feng Liu, Zuo-Quan Jiang, and Stephen R. Forrest*

The paucity of near-infrared (NIR) organic materials with high absorption at long wavelengths, combined with large diffusion lengths and charge mobilities, is an impediment to progress in achieving high-efficiency organic tandem solar cells. Here a subcell is employed within a series tandem stack that comprises a solution-processed ternary blend of two NIR-absorbing nonfullerene acceptors and a polymer donor combined with a small-molecular-weight, short-wavelength fullerene-based subcell grown by vacuum thermal evaporation. The ternary cell achieves a power conversion efficiency of $12.6 \pm 0.3\%$ with a short-circuit current of $25.5 \pm 0.3 \text{ mA cm}^{-2}$, an open-circuit voltage of $0.69 \pm 0.01 \text{ V}$, and a fill factor of 0.71 ± 0.01 under 1 sun, AM 1.5G spectral illumination. The success of this device is a result of the nearly identical offset energies between the lowest unoccupied molecular orbitals (LUMOs) of the donors with the highest occupied molecular orbital (HOMO) of the acceptor, resulting in a high open-circuit voltage. A tandem structure with an antireflection coating combining these subcells demonstrates a power conversion efficiency of $15.4 \pm 0.3\%$.

Organic photovoltaics (OPVs) have the potential for producing low-cost and ubiquitous renewable energy in the future due to their reliance on abundant and environmentally friendly carbon-based materials. Furthermore, their ability to be deposited on flexible, lightweight, and transparent substrates provides a path to mass production via continuous roll-to-roll deposition.^[1] By stacking both large- and small-energy-gap cells into a tandem OPV, the efficiency can be improved by minimizing the thermalization losses.^[2–5] However, the relative lack of high-performance, small-energy-gap cells has impeded the progress in tandem solar cell efficiency.^[6–9] Recently, our group demonstrated an organic tandem solar cell with a power conversion efficiency (PCE) as high as

PCE = 15.0% under 1 sun, AM 1.5G spectral illumination.^[10] This result was based on the combination of a fullerene-based cell deposited via vacuum thermal evaporation (VTE), along with a solution-processed, two-component NIR nonfullerene acceptor (NFA) subcell absorbing between wavelengths of 650–850 nm with PCE $\approx 11\%$.^[11]

Although recent rapid developments of small-energy-gap NFAs provides opportunities to achieve high-efficiency NIR cells, only a few nonfullerene acceptors have significant absorption and wavelengths greater than 1000 nm.^[12–16] The successful design of narrow energy gap NFAs requires precise tuning of the energy levels while maintaining a sufficient heterojunction energy offset to efficiently drive the dissociation of excitons. In this context, ternary blend OPVs containing one additional electron donor or acceptor material are a promising way to overcome the efficiency bottleneck encountered by conventional binary cells.^[17–22] In this work, we use ternary blends of two NIR nonfullerene acceptors with a polymer donor to significantly reduce energy losses. A narrow energy gap nonfullerene acceptor, 4,4,10,10-tetrakis(4-hexylphenyl)-4,10-dihydrothieno[2'',3'':4',5']thieno[3',2':4,5]cyclopenta[1,2-*b*]thiophene-2,8-diyl)bis(2-(3-oxo-2,3-dihydroinden-5,6-difluoro-1-ylidene) malononitrile (TT-FIC)^[13] sharing a similar lowest unoccupied molecular orbital (LUMO) energy with a second acceptor 4,4,10,10-tetrakis(4-hexylphenyl)-5,11-(2-ethylhexyloxy)-4,10-dihydro-dithienyl[1,2-*b*:4,5*b*]benzodithiophene-2,8-diyl)bis(2-(3-oxo-2,3-dihydroinden-5,6-dichloro-1-ylidene)malononitrile (BT-CIC, absorption up to 1000 nm) is blended with the polymer PCE-10 (poly[4,8-bis(5-(2-ethylhexyl)thiophen-2-yl)benzo[1,2-*b*:4,5-*b'*]dithiophene-*co*-3-fluorothieno[3,4-*b*]thiophene-2-carboxylate]). The resulting small differences in offset energies (40 meV) between the LUMOs of the acceptors and the highest occupied molecular orbitals (HOMOs) of the donors, along with the significantly different energy gaps (by 0.11 eV) of the acceptors, result in an open-circuit voltage (V_{OC}) that is close to the maximum possible for this narrow energy gap system.

The PCE of the ternary cell is increased from $10.8 \pm 0.2\%$ in a BT-CIC:PCE-10 cell to $12.6 \pm 0.3\%$ in the BT-CIC:TT-FIC:PCE-10 ternary OPV. Furthermore, the short-circuit current density (J_{SC}) is increased from 22.3 ± 0.4 to $25.5 \pm 0.3 \text{ mA cm}^{-2}$. Importantly, the absorption of the ternary cell is extended to 1000 nm with the energy loss ($E_{loss} = E_g - qV_{OC}$ where E_g is the smaller energy gap of either the donor or acceptor) decreased from 0.64 to 0.55 eV.

Dr. Y. Li, X. Liu, Y. Qu, Prof. S. R. Forrest
Department of Electrical Engineering and Computer Science
University of Michigan
Ann Arbor, MI 48109, USA
E-mail: stevefor@umich.edu

J.-D. Lin, F.-P. Wu, Prof. Z.-Q. Jiang
Institute of Functional Nano & Soft Materials (FUNSOM)
Soochow University
Suzhou, Jiangsu 215123, P. R. China

Prof. F. Liu
Department of Physics and Astronomy, and Collaborative Innovation
Center of IFSA (CICIFSA)
Shanghai Jiaotong University
Shanghai 200240, P. R. China

DOI: 10.1002/adma.201804416

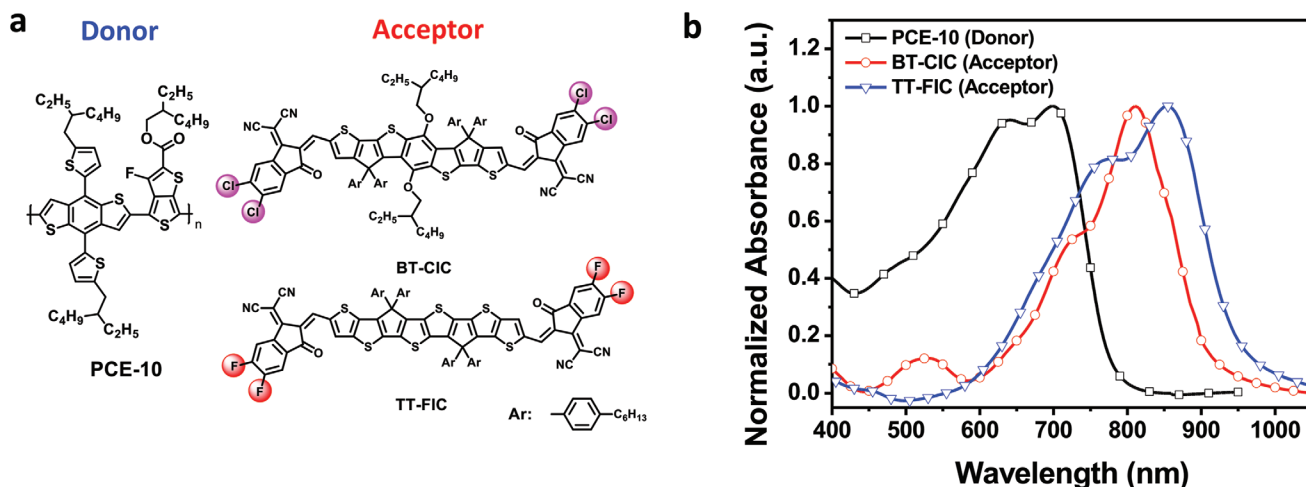


Figure 1. a) Molecular structural formulae of PCE-10, BT-CIC, and TT-FIC used in the single-junction and tandem cells. b) UV-vis absorption spectra of PCE-10, BT-CIC, and TT-FIC thin films.

Although the PCE of ternary single-junction solar cells exceeds 12%, their light absorption remains limited by the very thin active layer (≈ 100 nm) due to the low charge carrier mobility of the organic semiconductors. While energy conversion can be improved with a multijunction architecture, the potential of ternary subcells in multijunction devices has not yet been substantially explored.^[17] Here, we demonstrate a tandem structure with an antireflection coating (ARC), combining both binary- and ternary-based OPVs, reaching PCE = $15.4 \pm 0.3\%$ under 1 sun, AM 1.5G simulated illumination (area = 2 mm^2). This suggests the potential for the use of ternary subcells in multijunction devices that can achieve even higher efficiencies than reported here.

The chemical structures of the PCE-10, BT-CIC, and TT-FIC are shown in Figure 1a. The synthetic route for TT-FIC is shown in Scheme S1 in the Supporting Information. All materials are soluble in chloroform (CF), chlorobenzene (CB), and *ortho*-dichlorobenzene (*o*-DCB). Thin film absorption spectra of PCE-10, BT-CIC, and TT-FIC are shown in Figure 1b. In contrast

to BT-CIC, the absorption spectrum of TT-FIC is redshifted by 50 nm, resulting in absorption between $\lambda = 600$ and 1000 nm, and a small optical energy gap of 1.24 eV. The absorption of blended films with different weight ratios of TT-FIC is shown in Figure 2a. With increasing TT-FIC content, the absorption between 600 and 1000 nm in the ternary blends gradually increases due to the change in NIR absorption by the addition of TT-FIC.

Cyclic voltammetry in Figure S1 (Supporting Information) gives the HOMO (E_{HOMO}) and LUMO (E_{LUMO}) energies of $-5.42 (\pm 0.02)$ and $-4.13 (\pm 0.02)$ eV, respectively, for TT-FIC, and $-5.49 (\pm 0.02)$ and $-4.09 (\pm 0.02)$ eV for BT-CIC. TT-FIC shows a lower HOMO–LUMO energy gap (1.29 eV) than BT-CIC (1.40 eV, see Figure 2b), which is consistent with optical measurements. However, TT-FIC exhibits shallower HOMO and deeper LUMO energies compared with BT-CIC, which leads to a reduction of V_{OC} in TT-FIC-based binary OPVs.

The morphologies of both the binary and ternary blends were characterized by grazing-incidence X-ray diffraction. As shown

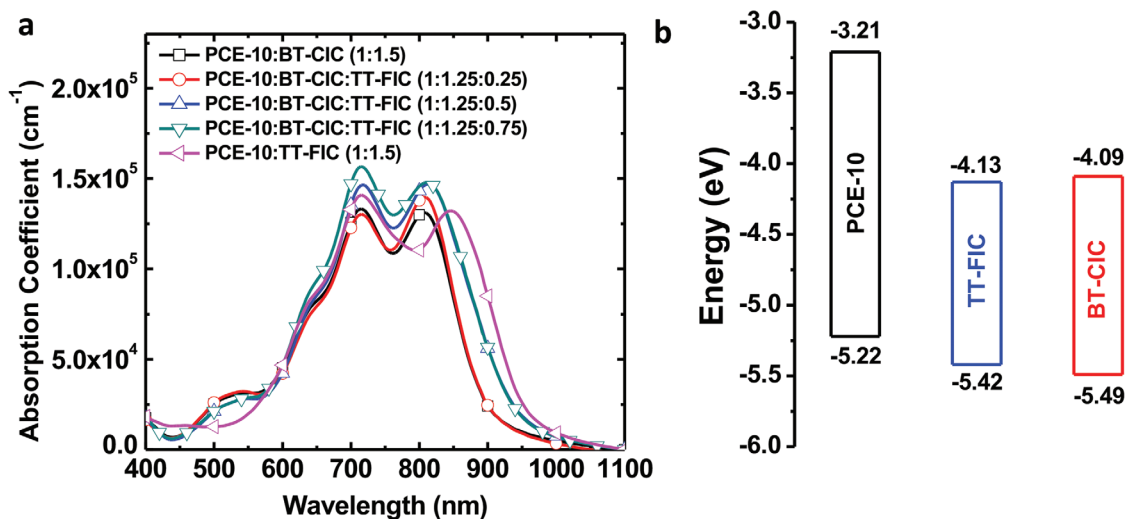


Figure 2. a) UV-vis absorption spectra of ternary blend films. b) Energy level diagram of PCE-10, BT-CIC, and TT-FIC relative to vacuum obtained from cyclic voltammetry. Numbers are in electron volts relative to the vacuum level.

in Figure S2 (Supporting Information), the two binary blends show quite different solid-state ordering. The PCE-10:BT-CIC blends show more intense diffraction features with contributions from both PCE-10 and BT-CIC compared to PCE-10:TT-FIC. This indicates that the crystallization of both PCE-10 and TT-FIC is decreased in the blends. In ternary blends, both PCE-10:BT-CIC:TT-FIC (1:1.25:0.25, w/w/w) and PCE-10:BT-CIC:TT-FIC (1:1.25:0.5, w/w/w) showed similar structural ordering compared to PCE-10:BT-CIC (1:1.5, w/w), but further increasing the content of TT-FIC to 0.75 caused only a small decrease in diffraction peak intensity. This suggests that PCE-10 and BT-CIC are guiding the morphology of the ternary mixture. The TT-FIC molecules locate between PCE-10 and BT-CIC domains while leaving the size and structure of the PCE-10 and BT-CIC domains unchanged. Therefore, electron transport and collection occur through the BT-CIC instead of TT-FIC. Thus, the TT-FIC functions as a sensitizer. This is one possible reason that the addition of TT-FIC to PCE10:BT-CIC does not influence V_{OC} (see the following).

Phase segregation within the blends was further studied by resonant soft X-ray diffraction, with results in Figure S2c (Supporting Information). Both of the PCE-10:BT-CIC (1:1.5, w/w) and PCE-10:TT-FIC (1:1.5) blends show a multi-length scaled morphology, with one peak at $Q = 0.085 \text{ \AA}^{-1}$ (corresponding to a distance of 74 nm) and another at 0.025 \AA^{-1} (250 nm), suggesting structure at a dimension of hundreds of nanometers. In contrast, a single diffraction peak was observed in all three ternary blends, where PCE-10:BT-CIC:TT-FIC (1:1.25:0.5) exhibits the smallest scale for phase separation (74 nm) compared to the PCE-10:BT-CIC:TT-FIC (1:1.25:0.25, 94 nm) and PCE-10:BT-CIC:TT-FIC (1:1.25:0.75, 106 nm). The PCE-10:BT-CIC:TT-FIC blend film shows a high intensity peak at 0.067 \AA^{-1} (corresponding to a distance of 94 nm) in Figure S2 (Supporting Information), while the PCE-10:BT-CIC:TT-FIC blend has a lower intensity peak at 0.085 \AA^{-1} (corresponding to a distance of 74 nm). The higher intensity indicates greater domain purity, but the enlarged phase separation for PCE-10:BT-CIC:TT-FIC blend is inferior for charge extraction. Therefore, it is hard to predict the J_{SC} only from the morphology study.

Atomic force microscopy (AFM) images of binary and ternary blends are shown in Figure S3 (Supporting Information), where

the PCE-10:BT-CIC:TT-FIC (1:1.25:0.5) blend has a root-mean-square roughness of 0.79 nm, compared with 1.15 nm for the PCE-10:BT-CIC:TT-FIC (1:1.25:0.25, w/w/w) and 0.91 nm for PCE-10:BT-CIC:TT-FIC (1:1.25:0.75, w/w/w) blends.

Ternary OPVs were fabricated with the device structure: indium tin oxide (ITO)/poly(3,4-ethylenedioxythiophene):poly(styrene sulfonate) (PEDOT:PSS) (50 nm)/PCE-10:BT-CIC:TT-FIC (1:1.25: x , 95 nm)/1,3,5-tri(*m*-pyridin-3-ylphenyl)benzene (TmPyPB) (5 nm)/Ag (100 nm). To systematically study the effects of the blend ratios, we also prepared a binary cell with the structure: ITO/PEDOT:PSS (50 nm)/PCE-10:TT-FIC (1:1.5, 100 nm)/ZnO (35 nm)/Ag(100 nm). The ZnO nanoparticles (NPs) were used for the electron-transporting layer to improve the contact between TmPyPB and PCE-10:TT-FIC. Details of fabrication are found in the "Experimental Section."

The current-density–voltage (J – V) characteristics of PCE-10:BT-CIC:TT-FIC (1: x : y) blends are plotted in Figure 3a, with a summary of device performance in Table 1. Compared to the BT-CIC, the TT-FIC-based binary device shows increased J_{SC} (24.7 ± 0.6 vs $22.3 \pm 0.4 \text{ mA cm}^{-2}$), but decreased V_{OC} (0.650 ± 0.004 vs $0.695 \pm 0.004 \text{ V}$) and fill factor ($FF = 0.67 \pm 0.01$ vs 0.70 ± 0.01). The higher J_{SC} is due to absorption deeper into the NIR for TT-FIC. However, the increased LUMO energy of TT-FIC and decreased blend crystallization result in the lower V_{OC} and FF. In contrast to the PCE-10:BT-CIC binary cell, the incorporation of TT-FIC into the PCE-10:BT-CIC blend significantly increases J_{SC} , without changes to V_{OC} and FF. The trend in the performance of the ternary cells versus acceptor blending ratio is shown in Figure 3b. The optimized devices comprised PCE-10:BT-CIC:TT-FIC (1:1.25:0.5), with $PCE = 12.6 \pm 0.3\%$, $V_{OC} = 0.693 \pm 0.005 \text{ V}$, $J_{SC} = 25.5 \pm 0.4 \text{ mA cm}^{-2}$, and $FF = 0.71 \pm 0.1$. This is more than a 15% enhancement in PCE compared with the reference cell. We also note that this efficiency is among the highest value reported for ternary blend OPVs so far. Figure 4a shows a PCE histogram for a population of 50 devices. The efficiencies fall in a narrow range between 12.0% and 12.6% with the mean value of 12.4%.

The external quantum efficiencies (EQE) versus wavelength are shown in Figure 4b for several different ternary blend

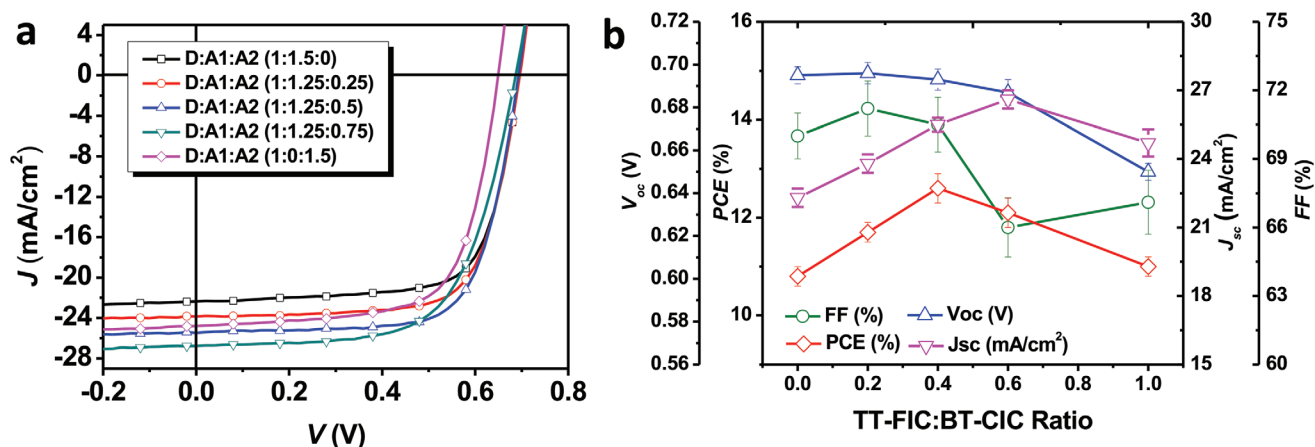


Figure 3. a) Current-density–voltage characteristics of ternary cells based on PCE-10, BT-CIC, and TT-FIC. b) V_{OC} , J_{SC} , FF, and PCE of optimized ternary cells as functions of TT-FIC:BT-CIC blend ratios, under 1 sun intensity (100 mW cm^{-2}), AM 1.5G simulated illumination.

Table 1. Operating characteristics of OPVs under simulated of AM 1.5G, 100 mW cm⁻², illumination.

PCE-10:BT-CIC:TT-FIC	J_{sc}^a [mA cm ⁻²]	V_{oc} [V]	FF	PCE ^b [%]
1:1.5:0	22.3 ± 0.4 (21.2)	0.695 ± 0.004	0.70 ± 0.01	10.8 ± 0.2
1:1.25:0.25	23.8 ± 0.4 (23.3)	0.696 ± 0.005	0.71 ± 0.01	11.7 ± 0.2
1:1.25:0.5	25.5 ± 0.3 (24.4)	0.693 ± 0.005	0.71 ± 0.01	12.6 ± 0.3
1:1.25:0.75	26.6 ± 0.4 (24.9)	0.687 ± 0.006	0.66 ± 0.01	12.1 ± 0.3
1:0:1.5	24.7 ± 0.6 (23.8)	0.650 ± 0.004	0.67 ± 0.01	10.8 ± 0.2

^a)The values in parentheses are calculated from the integral of the EQE spectrum; ^b)The average value is based on measurement of 50 devices.

ratios. Increasing the TT-FIC content gradually increases EQE at long wavelengths. The integrated photocurrents from the EQE spectra are consistent with the J_{SC} values obtained using the solar simulator (see Table 1), confirming the high photocurrent generation efficiency in the ternary devices. Importantly, the EQE of the PCE-10:BT-CIC:TT-FIC (1:1.25:0.5, 95 nm) cell reaches 75%, between $\lambda = 650$ and 900 nm, while leaving a transparency window at $\lambda < 600$ nm. This makes the device suitable for use as the back subcell (i.e., the cell adjacent to the reflective cathode) in a series-connected tandem OPV.

A 2-([7-(4-N,N-ditolyaminophenyl)-2,1,3-benzothiazol-4-yl]methylene)malononitrile (DTDCPB):C₇₀ (1:2, w/w) blend was chosen as the active region of the front subcell of the tandem due to its response in the wavelength range from 350 to 600 nm.^[23] Therefore, DTDCPB:C₇₀ and PCE-10:BT-CIC:TT-FIC subcells have complementary absorption spectra, as required in tandem solar cells. The tandem device structure is shown in Figure 5a, where the DTDCPB:C₇₀ subcell grown by VTE and the solution-processed PCE-10:BT-CIC:TT-FIC subcell were series connected with a charge recombination zone comprising bathophenanthroline (BPhen):C₆₀ (8 nm)/Ag NP/PEDOT:PSS (50 nm). The BPhen:C₆₀ serves as an exciton-blocking layer,^[24] the PEDOT:PSS functions as both a hole-transporting layer and a cap that protects the VTE-grown front subcell from penetration by the solution used in processing the back subcell. The 3 Å thick Ag nanoparticle layer promotes charge recombination.^[25] The simulated relative absorbed power distribution is displayed in Figure 5a. The ternary back cell absorbs in the NIR from 700 to 950 nm, while the largest absorption occurs between $\lambda = 350$ and 700 nm in the front cell. The charge recombination zone is nearly optically lossless.

Figure 5b presents the J - V characteristics of the tandem cells, with details summarized in Table 2. As a result of insufficient light absorption by the DTDCPB:C₇₀ front subcell that lacks a reflecting metal cathode, thicker films are required to balance currents between the subcells compared to previously reported 80 nm thick single-junction structures.^[23] Figure S4 (Supporting Information) shows the J - V characteristics of the tandem cells with various DTDCPB:C₇₀ thicknesses. The optimized tandem cell with 170 nm DTDCPB:C₇₀ together with the 85 nm PCE-10:BT-CIC:TT-FIC back subcell exhibits $J_{SC} = 13.3 \pm 0.2$ mA cm⁻², $V_{OC} = 1.56 \pm 0.01$ V, FF = 0.71 ± 0.01, and PCE = 14.7 ± 0.3% measured with mask to eliminate edge effects.^[26,27] In contrast to our previous work^[10] (see Table 2), the J_{SC} for this tandem OPV has been increased due to the redshifted absorption of the ternary subcell. The performance of the 9 mm² tandem cells is found in Table 2, showing ≈3% (relative) lower efficiency than the 2 mm² devices. We also note that the V_{OC} of the tandem equals the sum of the V_{OC} of the single-junction cells from which it is comprised, indicating the lossless charge recombination by the Ag NPs.

Figure 5c shows a PCE histogram of a population of 32 optimized tandem devices. The efficiencies fall in a narrow range between 14.2% and 14.8%. An ARC layer consisting of a 120 nm MgF₂ (index of refraction, $n_{MgF_2} = 1.38 \pm 0.01$) and 130 nm SiO₂ deposited at glancing incidence to lower the refractive index to $n_{SiO_2} = 1.12 \pm 0.03$ was used to reduce optical losses and further increase the efficiency.^[28] The reflection ratio of the glass substrate with and without the ARC decreases by ≈4% between $\lambda = 400$ and 1000 nm (see Figure S5 in the Supporting Information). The ARC tandem cell shows an increased J_{SC} from 13.3 ± 0.2 to 13.8 ± 0.3 mA cm⁻², thus leading to an increase to PCE = 15.4 ± 0.3%.

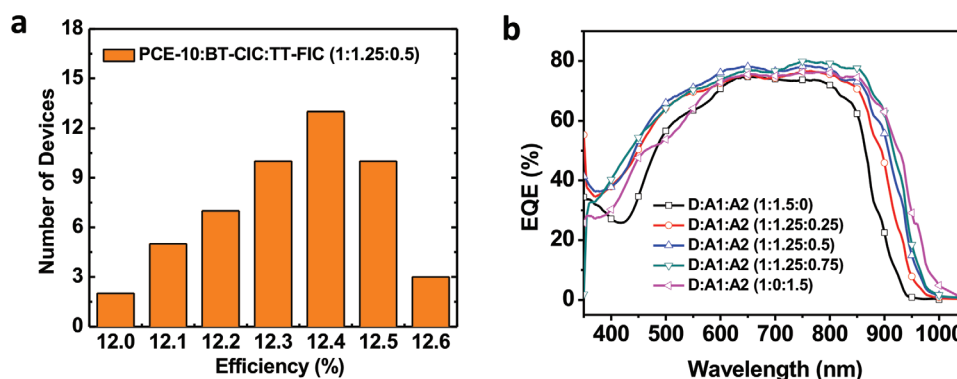


Figure 4. a) Efficiency histogram for a population of 50 optimized ternary cells, and b) external quantum efficiency (EQE) spectra of ternary cells with various blending ratios.

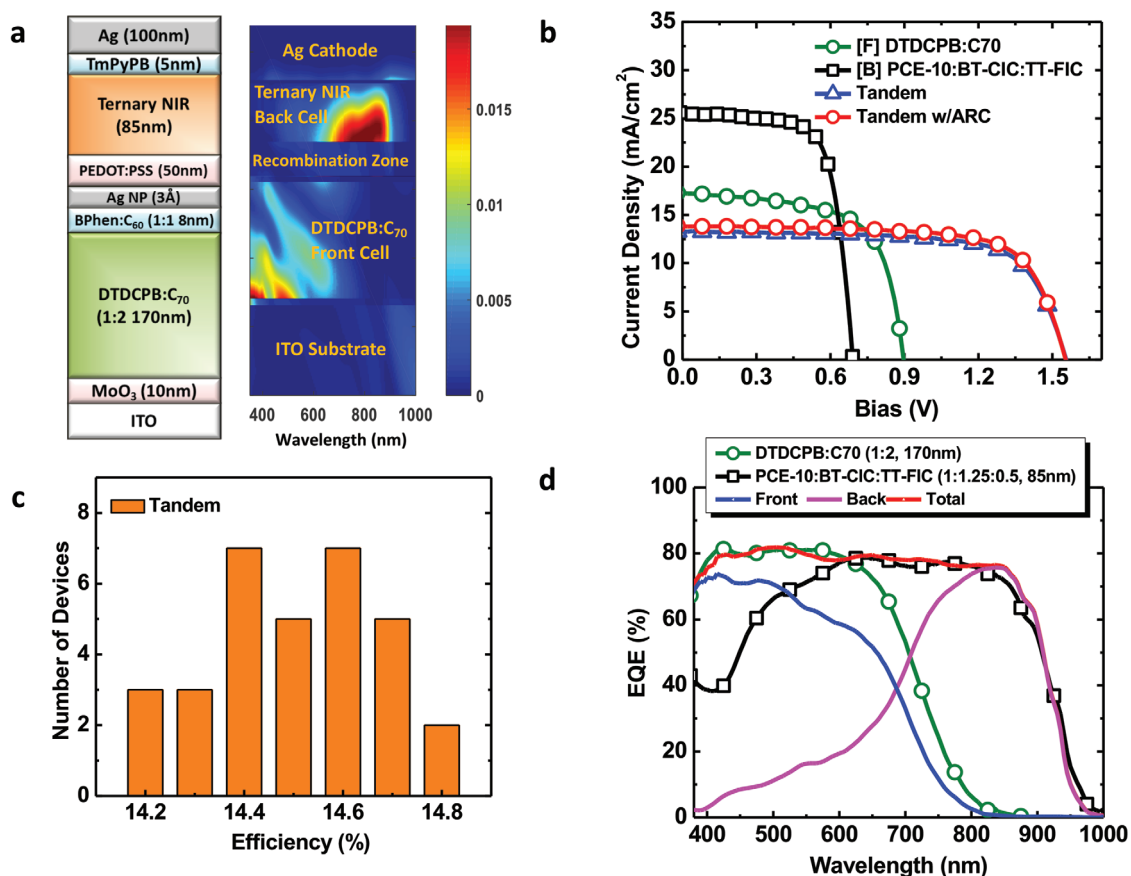


Figure 5. a) Schematic of the tandem device showing optimized layer thicknesses and compositions. Also shown is the optical field intensity distribution within the cell obtained via the transfer matrix method. Note the nonoverlapping spectra in the front (near the ITO) and back subcells leading to good current balance. b) Current-density–voltage characteristics of the optimized tandem cell together with the single-junction subcells. c) Efficiency histogram for a population of 32 optimized tandem cells (2 mm² effective area, without antireflection coatings), and d) external quantum efficiency (EQE) spectra of the tandem and discrete subcells. The symbols are for the discrete single junctions, while the magenta and blue lines are for the subcells in the stack obtained under light bias at wavelengths of 780 and 365 nm, and electrical bias of 0.45 and 0.75 V. The red line is the sum of the two measured EQEs obtained using light bias.

The J – V characteristics of tandem cells without ARC were also measured under incident light intensities varied from 12 to 100 mW cm^{−2} using neutral density filters, with results shown in Figure S6 (Supporting Information). The J_{SC} is proportional to light intensity, indicating a lack of space charge build-up within the two subcells and in the charge recombination zone. The FF of the tandem devices increased

to 75% under low light intensity, which is due to reduced charge recombination. The EQE spectra of the single-junction DTDCPB:C₇₀ (1:2, 170 nm) and PCE-10:BT-CIC:TT-FIC (1:1.25:0.5, 85 nm) cells are plotted in Figure 5d (circles and squares, respectively), as well as the individual subcells under illumination conditions experienced in the tandem cell.

Table 2. Discrete subcell and tandem device performances.

Device	J_{SC} [mA cm ^{−2}]	V_{OC} [V]	FF	PCE [%]
[Back] PCE-10:BT-CIC:TT-FIC (1:1.25:0.5, 85 nm)	24.8 ± 0.3	0.69 ± 0.01	0.70 ± 0.01	12.4 ± 0.2
[Front] DTDCPB:C ₇₀ (1:2, 170 nm)	17.1 ± 0.3	0.90 ± 0.01	0.65 ± 0.01	10.0 ± 0.2
[Tandem] (w/ternary NIR subcells, 2 mm ²) ^{a)}	13.3 ± 0.2 (13.0) ^{b)}	1.56 ± 0.01	0.71 ± 0.01	14.7 ± 0.3
[Tandem] (w/binary NIR subcells, 2 mm ²) ^{c)}	12.7 ± 0.2	1.59 ± 0.01	0.71 ± 0.01	14.3 ± 0.3
[Tandem] (w/ternary NIR subcells, 9 mm ²) ^{a)}	12.8 ± 0.3 (12.6) ^{b)}	1.56 ± 0.01	0.71 ± 0.01	14.2 ± 0.3
[Tandem] (ternary cells + ARC, 2 mm ²) ^{a)}	13.8 ± 0.3 (13.5) ^{b)}	1.56 ± 0.01	0.71 ± 0.01	15.4 ± 0.3

^{a)}The J_{SC} values are measured from devices using masks. The details of the measurements are found in the “Experimental Section”; ^{b)}The values in parentheses are calculated from the integral of the EQE spectrum using light bias with electrical bias corrected. The details of the measurement are found in the “Experimental Section” and Supporting Information; ^{c)}The data from ref. [4]. J_{SC} values are measured from the devices without masks.

Measuring the EQE for a tandem cell is significantly more challenging compared to single-junction solar cells.^[29,30] Here, we measure the EQE of the individual subcells using both an optical and electrical bias (see the Supporting Information for details). As shown in Figure 5d, the subcells in the tandem architecture with the ARC absorb between $\lambda = 350$ and 1000 nm, both exhibiting a peak EQE ≈ 75 . The DTDCPB:C₇₀ (1:2, 170 nm) cell in the tandem exhibits a reduced EQE at $400 < \lambda < 700$ nm compared to the single-junction cell at the same thickness due to residual absorption by the PCE-10:BT-CIC:TT-FIC cell. The integrated $J_{SC} = 13.4$ mA cm⁻² for the front subcell and $J_{SC} = 13.5$ mA cm⁻² for the back subcell, leading to balanced current generation in each subcell. Interestingly, the sum of the quantum efficiencies of the front and back subcells in the tandem features a nearly wavelength-independent quantum efficiency of $\approx 80\%$ from $\lambda = 400$ to 1000 nm.

The development of small-energy-gap materials is essential to the progress of OPV technology, although there exists trade-offs between E_g and E_{loss} that ultimately limits their performance.^[9] Introducing a third NIR absorber into the active region appears to balance this limitation, since ternary systems benefit by improving both the J_{SC} through NIR absorption while reducing E_{loss} , thus increasing V_{OC} . In this work, the J_{SC} in the PCE-10:BT-CIC:TT-FIC ternary cell is significantly increased (from 22.3 to 25.5 mA cm⁻²), due to the increase in absorption between 600 and 1000 nm as TT-FIC is incorporated into the ternary blend. Additionally, the reduced phase separation in ternary blends increases the interfacial area between donors and acceptors, thus promoting exciton dissociation and giving rise to improved J_{SC} . Furthermore, the PCE-10:BT-CIC:TT-FIC-based ternary cell shows a decreased E_{loss} compared to the PCE-10:BT-CIC binary cell (from 0.64 to 0.55 eV). This small E_{loss} is possibly due to the decreased HOMO energy offset with the NFAs and PCE-10 compared to BT-CIC. Previous studies have shown that minimizing the offset energies leads to a reduction in E_{loss} .^[31–33]

Compared to the PCE-10:BT-CIC:TT-FIC (1:1.25:0.5) ternary cell, the TT-FIC-based binary device shows decreased J_{SC} (24.7 ± 0.6 vs 25.5 ± 0.4 mA cm⁻²), V_{OC} (0.650 ± 0.004 vs 0.693 ± 0.005 V), and fill factor (FF = 0.67 ± 0.01 vs 0.71 ± 0.01). For the series-connected multijunction devices, the voltage across the device is equal to the sum of the voltages across each subcell according to Kirchhoff's law. In other words, the increased V_{OC} of the ternary subcell results in a higher V_{OC} in the tandem device. Moreover, the FFs of the tandem cells rely on the FFs of each subcell. Therefore, the higher FF of the ternary subcell further improves the performance of tandem. Based on these considerations, the efficiency of tandem device is further increased by using ternary versus binary subcells.

The PCE-10:BT-CIC:TT-FIC ternary device can also achieve EQE = 75% between the wavelengths of $\lambda = 650$ and 900 nm, in addition to a transparency window between $\lambda = 350$ and 650 nm. The tandem OPV that comprises the VTE-deposited fullerene binary subcell and the solution-processed ternary NIR subcell shows a higher PCE = $15.4 \pm 0.3\%$ with obvious increases in J_{SC} compared to the reference cell.^[10] The higher J_{SC} is attributed to the extended absorption of the ternary subcell. This suggests that the addition of ternary subcells with complementary absorption in tandem OPVs is a means for increasing PCE. Furthermore, a high FF = 0.71 was achieved

in our tandem device. This is attributed to the lower light intensity in ternary subcell, resulting in reduced current density and bimolecular recombination (see Figure S7 in the Supporting Information). Since submitting our paper, Meng et al. reported a double ternary-junction tandem cell with 17.3% PCE.^[34] An unexplained result is the higher voltage of the tandem cell compared to the sum of the individual subcells that could be due to several factors such as different light intensities used for the various measurements. Nevertheless, this result points to the benefits that can be achieved using ternary subcells, as demonstrated in this work.

In summary, we demonstrated a highly efficient NIR-absorbing ternary solar cell with a polymer donor (PCE-10) and two NIR-absorbing NFAs (BT-CIC and TT-FIC). The second NFA component in the ternary blend extends absorption across a broader spectral range, achieves improved film morphology, and ultimately reduces energy losses. The optimized PCE-10:BT-CIC:TT-FIC-based single-junction cell exhibits PCE = $12.6 \pm 0.3\%$. The tandem device structure incorporating a ternary NFA and a fullerene binary subcell shows PCE = $15.4 \pm 0.3\%$. This work points to a simple means for developing OPVs with very high efficiency, low E_{loss} NIR solar cells.

Experimental Section

Materials: All devices were grown on patterned ITO substrates with a sheet resistance of $15 \Omega \text{ sq}^{-1}$. The NIR-absorbing acceptors, BT-CIC and TT-FIC, were synthesized here. Other materials were purchased from commercial suppliers: MoO₃ (Acros Organics); DTDCPB, BPhen, and TmPyPB (Luminescence Technology Corp.); C₇₀ (SES Research); C₆₀ (MER Corp.); PEDOT:PSS (Clevios P VP Al. 4083, Heraeus); PCE-10 (1-Material); Ag (Alfa Aesar). DTDCPB, C₆₀, and C₇₀ were purified once by temperature-gradient sublimation prior to deposition.

Single-Junction Solar Cell Fabrication: Prepatterned ITO on glass substrates was cleaned using a series of detergents and solvents followed by CO₂ snow cleaning and exposed to ultraviolet–ozone for 15 min before growth.^[35] The PEDOT:PSS was filtered once with a 0.45 μm Nylon syringe filter prior to use, and then spin-coated onto the substrate at 5000 rpm for 60 s. The active layer, PCE-10:BT-CIC:TT-FIC (1:x:y, w/w/w), was dissolved in CB:CF (9:1 by vol) with a concentration of 20 mg mL⁻¹. The solution was stirred overnight on a hot plate at 65 °C, and then spin-coated at 2000 rpm for 90 s to achieve a thickness of ≈ 95 nm. The samples were then transferred back to the vacuum chamber for deposition of TmPyPB and the Ag cathode. For the PCE-10:TT-FIC-based device, ZnO nanoparticles were used for an electron-transporting layer. The device areas of 2.0 and 9.0 mm² were defined by the overlap between the patterned ITO and the Ag cathode deposited through an ultrathin shadow mask (50 μm).

Tandem Solar Cell Fabrication: Prepatterned ITO on glass substrates was cleaned using a series of detergents and solvents followed by CO₂ snow cleaning and exposed to ultraviolet–ozone for 15 min before growth. The vacuum-deposited layers for the front cell were grown at $\approx 1 \text{ \AA s}^{-1}$ in a high vacuum chamber with a base pressure of 2×10^{-7} Torr. During co-deposition of the VTE-grown DTDCPB:C₇₀ (1:2, w/w) layer, the deposition rate of each material was monitored by individual crystal sensors to achieve the desired volume ratios. After growing the active layer, a recombination zone consisting of three layers, a 3 \AA thick Ag NP layer deposited on the BPhen:C₆₀ mixed (1:1, w/w), followed by spin-coating the PEDOT:PSS (Clevios P VP Al. 4083, Heraeus) was grown. The vacuum chamber was connected to glove boxes filled with ultrapure N₂ (O₂, H₂O < 0.1 ppm) where the solution processed layers were subsequently deposited. The back NIR cells were made according to the single-junction

procedure. The ARC was grown onto the glass substrate after the devices were complete. MgF₂ was deposited by VTE while the SiO₂ was grown by electron beam deposition with the substrate at an angle of 85° to the beam direction to achieve a low refractive index of 1.1.

Solar Cell Characterization: The current-density–voltage (*J*–*V*) characteristics and spectrally resolved EQE were measured in a glove box filled with ultrapure N₂ (<0.1 ppm). Light from a Xe lamp filtered to achieve a simulated AM 1.5G spectrum (ASTM G173-03) was used as the source for *J*–*V* measurements. The lamp intensity controlled by neutral density filters was calibrated using a standard Si reference cell (with a KG-2 filter) traceable to certification by the National Renewable Energy Laboratory (NREL). The illumination intensity was adjusted using neutral density filters. Each cell was measured under six different light intensities from 0.001 to 1 sun (100 mW cm⁻²). Errors quoted accounted for variations from three or more cells measured, as well as an additional systematic error of 5% for *J*_{SC} and PCE. The devices were masked with a metal aperture to define the active area of 0.012 ± 0.001 and 0.063 ± 0.001 cm⁻² and measured in a light-tight sample holder to minimize edge effects. This ensured that both the reference and test cells were collocated under the solar simulator during measurement. The EQE measurements were performed with devices underfilled by a 200 Hz chopped monochromated and focused beam from a Xe lamp. The current outputs from the devices as well as from a reference NIST-traceable Si detector were recorded using a lock-in amplifier. The EQE of the individual subcells in the tandem devices was measured by using both an optical and an electrical bias. There was an ≈2% difference between the integrated *J*_{SC} from light bias EQE measurements to that using the solar simulator with a mask. The details can be found in the Supporting Information.

Supporting Information

Supporting Information is available from the Wiley Online Library or from the author.

Acknowledgements

Y.L. and S.R.F. were funded in part by the Office of Energy Efficiency and Renewable Energy (EERE), U.S. Department of Energy, under Award Number DE-EE0006708, and by the Department of the Navy, Office of Naval Research under Award No. N00014-17-1-2211. This work was also supported by the National Natural Science Foundation of China (51873139).

Conflict of Interest

The authors declare no conflict of interest.

Keywords

bias illumination, high efficiency, nonfullerene acceptors, polymers

Received: July 11, 2018

Revised: September 3, 2018

Published online: October 1, 2018

[1] B. Qu, S. R. Forrest, *Appl. Phys. Lett.* **2018**, *113*, 053302.

[2] J. Y. Kim, K. Lee, N. E. Coates, D. Moses, T.-Q. Nguyen, M. Dante, A. J. Heeger, *Science* **2007**, *317*, 222.

[3] A. Hadipour, B. de Boer, J. Wildeman, F. B. Kooistra, J. C. Hummelen, M. G. Turbiez, M. M. Wienk, R. A. Janssen, P. W. Blom, *Adv. Funct. Mater.* **2006**, *16*, 1897.

- [4] J. Gilot, M. M. Wienk, R. A. J. Janssen, *Adv. Mater.* **2010**, *22*, E67.
- [5] X. Che, X. Xiao, J. D. Zimmerman, D. Fan, S. R. Forrest, *Adv. Energy Mater.* **2014**, *4*, 1400568.
- [6] L. Dou, J. You, J. Yang, C.-C. Chen, Y. He, S. Murase, T. Moriarty, K. Emery, G. Li, Y. Yang, *Nat. Photonics* **2012**, *6*, 180.
- [7] L. Dou, Y. Liu, Z. Hong, G. Li, Y. Yang, *Chem. Rev.* **2015**, *115*, 12633.
- [8] Y. Li, J. Zou, H.-L. Yip, C.-Z. Li, Y. Zhang, C.-C. Chueh, J. Intemann, Y. Xu, P.-W. Liang, Y. Chen, A. K. Y. Jen, *Macromolecules* **2013**, *46*, 5497.
- [9] Y. Li, L. Zhong, B. Gautam, H.-J. Bin, J.-D. Lin, F.-P. Wu, Z. Zhang, Z.-Q. Jiang, Z.-G. Zhang, K. Gundogdu, Y. Li, L.-S. Liao, *Energy Environ. Sci.* **2017**, *10*, 1610.
- [10] X. Z. Che, Y. X. Li, Y. Qu, S. R. Forrest, *Nat. Energy* **2018**, *3*, 422.
- [11] Y. Li, J.-D. Lin, X. Che, Y. Qu, F. Liu, L.-S. Liao, S. R. Forrest, *J. Am. Chem. Soc.* **2017**, *139*, 17114.
- [12] H. Yao, Y. Cui, R. Yu, B. Gao, H. Zhang, J. Hou, *Angew. Chem., Int. Ed.* **2017**, *56*, 3045.
- [13] Z. Yao, X. Liao, K. Gao, F. Lin, X. Xu, X. Shi, L. Zuo, F. Liu, Y. Chen, A. K. Y. Jen, *J. Am. Chem. Soc.* **2018**, *140*, 2054.
- [14] S. Dai, T. Li, W. Wang, Y. Xiao, T. K. Lau, Z. Li, K. Liu, X. Lu, X. Zhan, *Adv. Mater.* **2018**, *30*, 1706571.
- [15] F. Liu, Z. Zhou, C. Zhang, J. Zhang, Q. Hu, T. Vergote, F. Liu, T. P. Russell, X. Zhu, *Adv. Mater.* **2017**, *29*, 1606574.
- [16] Z. Xiao, X. Jia, D. Li, S. Wang, X. Geng, F. Liu, J. Chen, S. Yang, T. P. Russell, L. Ding, *Sci. Bull.* **2017**, *62*, 1494.
- [17] L. Lu, M. A. Kelly, W. You, L. Yu, *Nat. Photonics* **2015**, *9*, 491.
- [18] Q. An, F. Zhang, J. Zhang, W. Tang, Z. Deng, B. Hu, *Energy Environ. Sci.* **2016**, *9*, 281.
- [19] H. Fu, Z. Wang, Y. Sun, *Solar RRL* **2018**, *2*, 1700158.
- [20] T. Liu, Y. Guo, Y. Yi, L. Hou, X. Xue, X. Sun, H. Fu, W. Xiong, D. Meng, Z. Wang, F. Liu, T. Russell, Y. Sun, *Adv. Mater.* **2016**, *28*, 10008.
- [21] R. Yu, S. Zhang, H. Yao, B. Guo, S. Li, H. Zhang, M. Zhang, J. Hou, *Adv. Mater.* **2017**, *29*, 1700437.
- [22] D. Baran, R. S. Ashraf, D. A. Hanifi, M. Abdelsamie, N. Gasparini, J. A. Rohr, S. Holliday, A. Wadsworth, S. Lockett, M. Neophytou, C. J. Emmott, J. Nelson, C. J. Brabec, A. Amassian, A. Salleo, T. Kirchartz, J. R. Durrant, I. McCulloch, *Nat. Mater.* **2017**, *16*, 363.
- [23] O. L. Griffith, X. Liu, J. A. Amonoo, P. I. Djurovich, M. E. Thompson, P. F. Green, S. R. Forrest, *Phys. Rev. B* **2015**, *92*, 085404.
- [24] A. N. Bartynski, C. Trinh, A. Panda, K. Bergemann, B. E. Lassiter, J. D. Zimmerman, S. R. Forrest, M. E. Thompson, *Nano Lett.* **2013**, *13*, 3315.
- [25] A. Yakimov, S. R. Forrest, *Appl. Phys. Lett.* **2002**, *80*, 1667.
- [26] H. J. Snaith, *Energy Environ. Sci.* **2012**, *5*, 6513.
- [27] Q. Burlingame, C. Coburn, X. Che, A. Panda, Y. Qu, S. R. Forrest, *Nature* **2018**, *554*, 77.
- [28] J. Q. Xi, J. K. Kim, E. F. Schubert, D. Ye, T. M. Lu, S.-Y. Lin, J. S. Juneja, *Opt. Lett.* **2006**, *31*, 601.
- [29] J. Gilot, M. M. Wienk, R. A. J. Janssen, *Adv. Funct. Mater.* **2010**, *20*, 3904.
- [30] W. Li, A. Furlan, K. H. Hendriks, M. M. Wienk, R. A. J. Janssen, *J. Am. Chem. Soc.* **2013**, *135*, 5529.
- [31] W. Li, K. H. Hendriks, A. Furlan, M. M. Wienk, R. A. J. Janssen, *J. Am. Chem. Soc.* **2015**, *137*, 2231.
- [32] K. Vandewal, Z. Ma, J. Bergqvist, Z. Tang, E. Wang, P. Henriksson, K. Tvingstedt, M. R. Andersson, F. Zhang, O. Inganäs, *Adv. Funct. Mater.* **2012**, *22*, 3480.
- [33] Y. Li, X. Liu, F.-P. Wu, Y. Zhou, Z.-Q. Jiang, B. Song, Y. Xia, Z.-G. Zhang, F. Gao, O. Inganäs, Y. Li, L.-S. Liao, *J. Mater. Chem. A* **2016**, *4*, 5890.
- [34] L. Meng, Y. Zhang, X. Wan, C. Li, X. Zhang, Y. Wang, X. Ke, Z. Xiao, L. Ding, R. Xia, H. L. Yip, Y. Cao, Y. Cheng, *Science* **2018**, *361*, 1094.
- [35] N. Wang, X. Tong, Q. Burlingame, J. Yu, S. R. Forrest, *Sol. Energy Mater. Sol. Cells* **2014**, *125*, 170.